FERMILAB-PUB-14-066-A

Draft version March 7, 2014
Preprint typeset using LaTeX style emulateapj v. 2/16/10

COSMIC REIONIZATION ON COMPUTERS I. DESIGN AND CALIBRATION OF SIMULATIONS

Nickolay Y. Gnedin[1,2,3]

Draft version March 7, 2014

ABSTRACT

Cosmic Reionization On Computers (CROC) is a long-term program of numerical simulations of cosmic reionization. Its goal is to model fully self-consistently (albeit not necessarily from the first principles) all relevant physics, from radiative transfer to gas dynamics and star formation, in simulation volumes of up to 100 comoving Mpc, and with spatial resolution approaching 100 pc in physical units. In this method paper we describe our numerical method, the design of simulations, and the calibration of numerical parameters. Using several sets (ensembles) of simulations in $20h^{-1}$ Mpc and $40h^{-1}$ Mpc boxes with spatial resolution reaching 125 pc at $z = 6$, we are able to match the observed galaxy UV luminosity functions at all redshifts between 6 and 10, as well as obtain reasonable agreement with the observational measurements of the Gunn-Peterson optical depth at $z < 6$.

Subject headings: cosmology: theory – cosmology: large-scale structure of universe – galaxies: formation – galaxies: intergalactic medium – methods: numerical

1. INTRODUCTION

Study of cosmic reionization has been highlighted by the last decadal survey as one of the most promising areas of astrophysical research in the current decade. Progress in this area directly influences many other fields of astrophysics, from thermal evolution of the Lyman-α forest to properties of early galaxies.

Because the observational constraints on reionization are limited, theoretical modeling, including numerical simulations, play a relatively larger part in reionization studies than in many other fields of modern astrophysics. Historically, simulations of reionization were mostly confined to two opposite limits: simulations of small spatial volumes with detailed treatment of relevant physics, or large volume simulations with simplified physical modeling (see Trac & Gnedin 2009, for a recent review). Both approaches suffer from serious limitations. Small box simulations can model individual ionizing sources with sufficient physical detail, but fail to account for the large-scale correlations between them. Large box simulations include these correlations, but, by ignoring gas dynamics, are not able to model ionizing sources self-consistently. The inability of the simulations to include all relevant scales resulted in a recent surge in semi-numerical and purely analytical approximate methods (Furlanetto et al. 2004; Furlanetto & Oh 2005; Choudhury & Ferrara 2005; Furlanetto et al. 2006; Choudhury & Ferrara 2006; Zahn et al. 2007a; Mesinger & Furlanetto 2007; Alvarez & Abel 2007; Shull & Venkatesan 2008; Zahn et al. 2011; Mitra et al. 2011; Venkatesan & Benson 2011; Mesinger et al. 2011; Kuhlen & Faucher-Giguère 2012; Alvarez & Abel 2012; Mitra et al. 2012; Zhou et al. 2013; Battaglia et al. 2013; Robertson et al. 2013; Kaurov & Gnedin 2013; Sobacchi & Mesinger 2014).

That's where Moore's Law comes to the rescue. The unrelenting exponential increase in the supercomputing power means that sooner or later the gap between small- and large-box simulations is going to be bridged. In fact, *this time is now* - the new generation of supercomputing platforms that have recently been and are planned to be deployed in the US[4], the so-called "peta-scale" platforms (since they get close to or exceed 10^{15} floating-point-operations per second), are particularly suitable for large-scale simulations of reionization that treat fully self-consistently the radiative transfer of ionizing radiation and gas dynamics.

Taking advantage of this technological progress, we have started a Cosmic Reionization On Computers (CROC) project that aims, over the course of several years, to produce numerical simulations of reionization that model fully self-consistently (albeit not necessarily from the first principles) all relevant physics, from radiative transfer to gas dynamics and star formation, in simulation volumes of up to 100 comoving Mpc and with spatial resolution approaching 100 pc in physical units.

In this first paper in a series, we focus primarily on the technical aspects of our simulations, such as the description of the numerical method, simulation design, and the calibration of simulation parameters. We present the original scientific results from our simulations in the subsequent publications.

2. NUMERICAL TOOLS

Our main simulation tool is the Adaptive Refinement Tree (ART) code (Kravtsov 1999; Kravtsov et al. 2002; Rudd et al. 2008). The ART code is an implementation of the Adaptive Mesh Refinement (AMR) technique with the Fully Threaded Tree data structure (Khokhlov 1998). It includes a wide range of physical processes that make it particularly suitable for modeling cosmic reionization. Specifically, the current version of the code includes the following physical ingredients (in addition to standard ingredients of gravity, dark matter, and gas dynamics).

Cooling and Heating of hydrogen and helium is computed "on the fly", taking into account all relevant processes in a time-dependent manner, without any assumptions of pho-

[1] Particle Astrophysics Center, Fermi National Accelerator Laboratory, Batavia, IL 60510, USA; gnedin@fnal.gov
[2] Kavli Institute for Cosmological Physics, The University of Chicago, Chicago, IL 60637 USA;
[3] Department of Astronomy & Astrophysics, The University of Chicago, Chicago, IL 60637 USA

[4] For example, "Stampede" at Texas Advanced Computing Center, "Kraken" at Oak Ridge National Lab, "Hopper" and "Edison" at Livermore-Berkeley Lab, "Mira" at Argonne National Lab, "Blue Waters" at NCSA, etc.

Operated by Fermi Research Alliance, LLC under Contract No. De-AC02-07CH11359 with the United States Department of Energy.

toionization or collisional equilibrium. Abundance of heavy elements is tracked self-consistently in ART, but, in a most general case, computing the full dependence of the cooling and heating functions on the incident radiation field is a complex task in itself, and cannot be currently implemented *exactly* in cosmological simulations, unless the radiation field is constant in space (Kravtsov 2003; Wiersma et al. 2009).

Since the latter is not a reasonable assumption during reionization or in the ISM of galaxies, ART uses an approximate method of Gnedin & Hollon (2012) that allows to compute the metallicity-dependent part of the cooling and heating functions for an arbitrary time-dependent and spatially-variable radiation field. ART, thus, is able to account for several physical effects that are missed in most other cosmological simulations codes, such as suppression of cooling in strong radiation fields, dependence of the LTE temperature on the radiation spectrum, etc (see Gnedin & Hollon (2012) for some representative examples).

Radiative Transfer of ionizing and ultraviolet radiation is currently implemented in ART using the Optically Thin Variable Eddington Tensor (OTVET) approximation of Gnedin & Abel (2001). While OTVET is an approximation, it has been extensively tested against exact schemes (Iliev et al. 2006a, 2009). The Iliev et al. tests underscored one undesirable feature of the original ART implementation of the OTVET method - excessive numerical diffusion around ionization fronts. The implementation of the OTVET scheme in ART was substantially revised after those tests, and the currently used approach eliminates numerical diffusion almost completely; a full description of our current implementation of OTVET is presented in Appendix C. Thus, OTVET remains a highly suitable method for modeling cosmic reionization (see Gnedin & Abel 2001, for detailed discussion of the limitations and inaccuracies of OTVET).

In our simulations, we include ionizing radiation from stars fully self-consistently (in a time-dependent and spatially-inhomogeneous manner), because it is the primary driver of the reionization process. Other sources of ionizing radiation (quasars, recombination radiation from helium that can ionize hydrogen, bremsstrahlung, etc) we only include in the cosmic background, because these sources are either weakly clustered (helium recombination radiation) or too rare to significantly affect the radiation field in a typical region of the universe (bright quasars). Both components - the radiation from local sources and the radiation from distant sources (i.e. cosmic background) - are treated separately in ART, and then combined together to derive a single solution of the radiative transfer equation (see Appendix C). The advantage of this approach is that it allows to account for the contribution of rare sources (like quasars) to the cosmic background without actually requiring an impractically large simulation volume.

Contributions from helium recombination and bremsstrahlung can be easily computed exactly. Our model for the *quasar contribution* is presented in Appendix A.

Of course, the cosmic background is only important if the mean free path of ionizing photons is sufficiently large, so that the radiation field from distant sources is comparable to or above the radiation field from local sources at a typical location in the universe.

Since we are running several independent realizations for each set of numerical parameters, the post-reionization evolution of the IGM would not be captured correctly if we computed the mean free path for the cosmic background from within one simulation box - periodic boundary conditions will extend that box over the whole universe, whereas it is supposed to represent just one sub-volume of the universe, and only the full set of independent realizations should be treated as a numerical model for the whole universe. Hence, we use the fit from Songaila & Cowie (2010) to account for Lyman Limit absorptions in the cosmic background; the background is then still subject to local absorptions inside shielded regions, as captured by the radiative transfer solver in Equation (C7). Radiation from local ionizing sources is absorbed fully self-consistently with the actually simulated gas distribution in the box (Eq. C4).

Molecular Hydrogen chemistry (both gas-phase and dust-based) can be followed in complete detail in ART (Gnedin & Kravtsov 2011). However, since spatial resolution of our simulations ($\gtrsim 100\,$pc) is too coarse to resolve the scale heights of galactic disks, it would make little sense to use the full molecular chemistry module in this work. Instead, we use the fitting formulae of Gnedin & Draine (2014, in preparation), derived from a large set of small-volume, high resolution simulations, to reliably account for the environmental dependence of the molecular gas on such ISM properties as dust-to-gas ratio or local interstellar radiation field. These fitting formulae are similar to the ones presented in Gnedin & Kravtsov (2011), but they also account for the overlap of damping wings of separate absorption lines in the Lyman-Werner band at high molecular column densities.

Star Formation cannot yet be modeled from the first principles in cosmological simulations, and needs to be implemented with a phenomenological "sub-grid" model. In the last several years an important observational advance has been made in understanding star formation on galactic scales. Both, local (Leroy et al. 2008; Bigiel et al. 2008; Bolatto et al. 2011; Bigiel et al. 2011; Leroy et al. 2012, 2013) and intermediate redshift (Genzel et al. 2010; Daddi et al. 2010; Tacconi et al. 2013) observational studies find that the star formation rate surface density on several-hundred-pc scales correlates well, and approximately linear, with the surface density of molecular gas. We use this observed correlation to define our star formation recipe in an entirely empirical manner,

$$\Sigma_{\rm SFR} = \frac{\Sigma_{\rm H_2}}{\tau_{\rm SF}}, \tag{1}$$

where $\Sigma_{\rm SFR}$ is the star formation rate surface density, $\Sigma_{\rm H_2}$ is the surface density of the molecular gas (including the contribution of helium), and $\tau_{\rm SF}$ is the molecular gas depletion time scale. We ignore the slightly sub- or super-linear slopes sometimes found in observations, since with our resolution we are only able to resolve a modest range of surface densities where the difference between an exactly linear and a slightly non-linear slopes is negligible.

The currently most widely accepted viewpoint is that the depletion time scale $\tau_{\rm SF} \approx 1-2\,$Gyr for normal star-forming galaxies. We use the value of $\tau_{\rm SF} = 1.5\,$Gyr as fiducial, and explore the effect of varying this parameter on our results below.

Stellar Feedback is implemented in our simulations with the current industry standard "blastwave" or "delayed cooling" model (Stinson et al. 2009; Governato et al. 2010; Agertz et al. 2011; Brook et al. 2012; Agertz et al. 2013a; Stinson et al. 2013). While this model is purely phenomenological, it is known to reproduce many of the observed properties of real galaxies well, and, hence, is an appropriate numerical tool at

present. The delay time-scale $\tau_{\rm BW}$ is a parameter that we vary as a part of the simulation calibration procedure. Our fiducial value of $\tau_{\rm BW} = 10\,{\rm Myr}$ is consistent with the usage of this feedback model in the field.

Ionizing Radiation from Stars is the dominant contributor to the global reionization process. The exact amount and spectrum of that radiation depend on stellar IMF and on local absorption inside the galaxy (usually quantified by "escape fractions"). For our modeled stars we use a fixed Kroupa IMF; the shape of the ionizing spectrum is adopted from Starburts99 modeling (Leitherer et al. 1999) and is plotted in Fig. 4 of Ricotti et al. (2002a). The total UV and ionizing luminosities of a single-age stellar population with mass m_* and metallicity Z_* can be computed with Starburst99; we fit numerical results with the following formula:

$$L_{\rm ion} = \epsilon_{\rm UV} 1.04 \times 10^{-4} \frac{m_* c^2}{Z_*^{0.1}(1 + 0.27 Z_*)} f(t),$$

where $f(t)$ is such that

$$\int_0^t f(t)\,dt = \frac{x\left(0.8 + x^2\right)}{1 + x\left(0.8 + x^2\right)},$$

and $x = t/(3\,{\rm Myr})$. At late times ($t \gg 10\,{\rm Myr}$) the ionizing emissivity from a single-age stellar population falls off with time more rapidly than UV light. Our fit behaves in between the ionizing and UV emissivities, since our OTVET implementation requires the same time-dependence of the source function for all radiation bands; that ansatz causes at most a few percent error.

The parameter $\epsilon_{\rm UV}$ is unity for the unattenuated stellar output. However, in a numerical simulation with finite spatial resolution some of the absorptions are not accounted for. For example, some of ionizing photons are absorbed in the parent molecular cloud from which stars form, further absorptions occur in the atomic ISM on scales below the effective resolution of the radiative transfer solver. To account for all of these unresolved photon losses, we include the $\epsilon_{\rm UV}$ factor and treat it as a free parameters of our model.

Both, our star formation model and the model for ionizing emissivity ignore Pop III stars, because it is well established that they contribute little to the reionization of the universe (Ricotti et al. 2002a,b; Wise & Abel 2008; Wise & Cen 2009; Wise et al. 2012; Muratov et al. 2013a,b).

3. DESIGN OF THE SIMULATIONS

3.1. *Resolution Requirements*

The very first simulations of reionization (Gnedin & Ostriker 1997; Gnedin 2000) demonstrated that, in order to account for all potential sources of ionizing radiation, all halos that can cool via atomic hydrogen line cooling ($M_{\rm tot} \gtrsim 10^9 {\rm M}_\odot$) need to be resolved. This conclusion was later confirmed by several other groups (Iliev et al. 2006b; Trac & Cen 2007; Zahn et al. 2007b; McQuinn et al. 2007; Trac et al. 2008; Pawlik et al. 2009) and is also consistent with the range of masses for Local Group dwarfs (e.g. Kravtsov 2009, and references therein). Such a requirement can be minimally satisfied with the mass resolution of $5 \times 10^6 {\rm M}_\odot$, which is equivalent of resolving a, say, $20h^{-1}$ Mpc box (in comoving units) with 512^3 dark matter particles.

Because in ART the number of dark matter particles throughout the simulation remains fixed, while cells of the adaptive mesh are created and destroyed dynamically, it is more convenient to quantify the resolution in terms of the number of dark matter particles. Each simulation starts with the same number of adaptive mesh cells as dark mater particles, to ensure the consistency of the mass resolution in two main gravitating components. As the simulation proceeds, the number of cells usually grows with time, so that by the end of the simulation the number of cells is a factor of several higher than the number of dark matter particles.

Our fiducial simulation series is presented in Table 1. Each of the simulations in the series is run with additional 6 levels of refinement, achieving the same cell size of 125 pc in proper units at $z = 6$ (145 pc at $z = 5$), with the actual spatial resolution being a factor ~ 3 worse. Such resolution is well matched to the range of scales on which the star formation model given by Equation (1) is observationally tested.

In this paper we only present results from $20h^{-1}$ Mpc and $40h^{-1}$ Mpc boxes. A simulation with the $80h^{-1}$ Mpc is currently feasible to complete on the largest available machines, but it is sufficiently computationally expensive (requiring 20-30 million CPU hours depending on the platform); with the computational resources available to us, we will only be able to afford one per year beginning with 2014.

3.2. *Running Sets of Simulations*

Even our largest "B80" simulations, with the $80h^{-1}$ Mpc box size, will be only marginally large enough for obtaining convergent results on the distribution of sizes of ionized regions or on observable properties of high redshift galaxies. Thus, in order to extend the reach of our simulations, we run sets of independent realizations of initial conditions for each particular choice of the box size and simulation parameters, accounting for the cosmic variance on the scale of the box size.

This variance is commonly referred to as the "DC mode". The ART code supports the DC mode in arbitrary cosmology without any approximations, following the method described in Gnedin et al. (2011). In fact, as has been shown in that paper, if a set of independent realizations with a given box size properly accounts for the DC mode, it becomes statistically equivalent to a simulation with a several times larger box.

Table 2 lists all sets of simulations that we present in this paper. We have performed several sets of $20h^{-1}$ Mpc that serve as our primary parameter exploration data. Most of the science results we extract from two sets of 3 independent realizations each of the $40h^{-1}$ Mpc box. We highlight in boldface the simulation sets that we consider "fiducial" - in the next section we justify that particular choice.

In order to distinguish individual realizations in each simulation set, we label them with capital letters. For example, the fiducial $20h^{-1}$ Mpc set (B20.sf1.uv2.bw10) includes

TABLE 1
SIMULATION PARAMETERS

Run	Box size (comoving)	Resolution (proper at $z = 6$)	Number of DM particles
"B20"	$20h^{-1}$ Mpc	125 pc	512^3
"B20HR"	$20h^{-1}$ Mpc	72 pc	1024^3
"B40"	$40h^{-1}$ Mpc	125 pc	1024^3
"B80"	$80h^{-1}$ Mpc	125 pc	2048^3

TABLE 2
COMPLETED SIMULATION SETS

Set Id	$\tau_{\rm SF}$ (Gyr)	$\epsilon_{\rm UV}$	$\tau_{\rm BW}$ (Myr)	Stopping redshift	Number of realizations
$20h^{-1}$ Mpc boxes					
B20.sf1.uv1.bw10	1.5	0.1	10	5	6 [A-F]
B20.sf1.uv2.bw10	1.5	0.2	10	5	6 [A-F]
B20.sf1.uv4.bw10	1.5	0.4	10	5	3 [D-F]
B20.sf1.uv2.bw40	1.5	0.2	40	5.7	3 [D-F]
B20.sf2.uv2.bw10	0.75	0.2	10	5.7	3 [D-F]
B20.sf2.uv2.bw40	0.75	0.2	40	7	3 [D-F]
B20HR.sf1.uv2.bw10	1.5	0.2	10	5.7	1 [B]
$40h^{-1}$ Mpc boxes					
B40.sf1.uv1.bw10	1.5	0.1	10	5	3 [A-C]
B40.sf1.uv2.bw10	1.5	0.2	10	5.5	3 [A-C]

six independent realizations A-F. A set B20.sf1.uv2.bw40 only includes 3 simulations D, E, and F, which have identical initial conditions to the simulations D, E, and F from the fiducial set B20.sf1.uv2.bw10. Hence, we have the ability to both compare simulations with identical initial conditions but varied physical parameters (like B20.sf1.uv2.bw10.D and B20.sf1.uv2.bw40.D) and simulations with identical physical parameters but different realizations of initial conditions (like B20.sf1.uv2.bw10.A and B20.sf1.uv2.bw10.B).

We also use comparison between $20h^{-1}$ Mpc and $40h^{-1}$ Mpc boxes as a rudimentary convergence test. Since every computed physical quantity may have different convergence requirements, we do not discuss numerical convergence in a separate sub-section, but rather include such discussion together with the calibration for each simulation parameter.

4. CALIBRATION OF THE SIMULATIONS

4.1. *Star Formation Model*

One of the largest existing observational data sets on the sources of reionization are the UV luminosity functions of high redshift galaxies. Matching them would validate our star formation and feedback models.

As our final simulation data, we combine the fiducial $20h^{-1}$ Mpc and $40h^{-1}$ Mpc sets (B20.sf1.uv2.bw10 and B40.sf1.uv1.bw10). Six independent realizations of the $20h^{-1}$ Mpc box are equivalent, by volume, to 0.75 of a single $40h^{-1}$ Mpc box, increasing our fiducial set from 3 to 3.75 $40h^{-1}$ Mpc boxes.

In order to predict UV luminosities of our model galaxies, we use the Flexible Spectral Population Synthesis (FSPS) code (Conroy et al. 2010; Conroy & Gunn 2010). One complication in computing stellar luminosities in far UV is a proper account of cosmic dust. A fully self-consistent dust model would require a complex and computationally expensive ray-tracing through the simulated galaxies, and is beyond the scope of this first paper. Instead, we adopt a simple but reasonable dust obscuration model, which we delegate to the appendix, as it has only modest effect on our results (and no effect at all at $z > 7$).

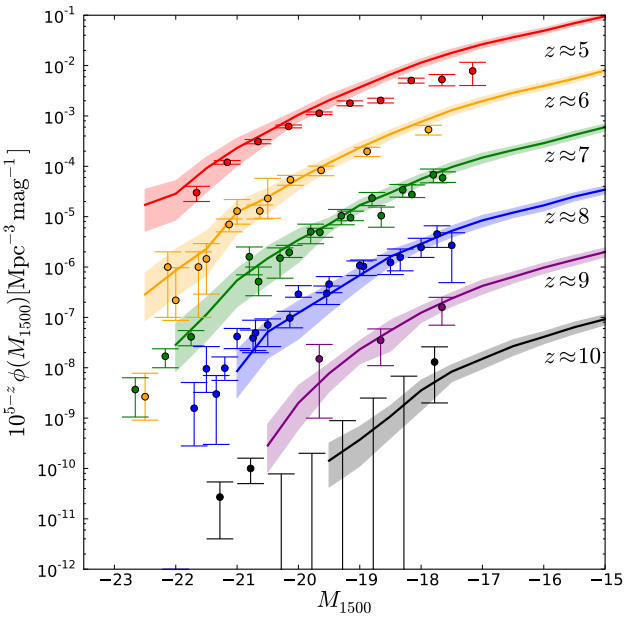

FIG. 1.— Ultraviolet galaxy luminosity functions from a combination of simulation sets B20.sf1.uv2.bw10 and B40.sf1.uv1.bw10 at 6 different redshifts. Lines with bands show the average luminosity functions with the rms variation over our effective 3.75 $40h^{-1}$ Mpc boxes (the error of the mean is, respectively, a factor of $\sqrt{3.75} = 1.9$ smaller). Circles with error-bars are a compilation of recent observational measurements (Bouwens et al. 2007, 2011; Oesch et al. 2012; Bradley et al. 2012; Schenker et al. 2013; Willott et al. 2013; Oesch et al. 2013a; Bowler et al. 2013; Oesch et al. 2013b). Different redshifts are shifted vertically by 1 dex for clarity.

Figure 1 presents the primary result of this paper - the evolution of the galaxy UV luminosity function between $z = 10$ and $z = 5$ from our simulations, and its comparison with the existing observational measurements[5]. A simple star formation model of Equation (1) is able to reproduce the observations for all $z > 5$. The agreement becomes worse at low luminosities at $z = 5$, and that is not particularly surprising - since our simulations maintain the fixed resolution in comoving units, the spatial resolution degrades as simulations evolve, and the feedback model becomes progressively less accurate, especially in the low mass galaxies.

The sensitivity of our star formation model to the numerical parameters $\tau_{\rm SF}$ and $\tau_{\rm BW}$ is explored in Figure 2. To compare apples and apples, we use only 3 independent realizations D-F from our fiducial set B20.sf1.uv2.bw10, and compare them with simulation sets B20.sf1.uv2.bw40, B20.sf2.uv2.bw10, and B20.sf2.uv2.bw40 (which only included 3 simulations D-F each, and were only continued to $z = 5.7$, to save computational resources). A longer time-scale $\tau_{\rm BW}$ for delayed cooling does have a significant effect on the simulated galaxies, but *not* a directly proportional one - luminosity functions for the set B20.sf1.uv2.bw40 match the fiducial set very well if shifted horizontally by about 0.5 magnitude, which corresponds to only a factor of 1.6. The sensitivity of our star formation model to the star formation time-scale $\tau_{\rm SF}$ (or, equivalently, to star formation efficiency) is stronger - a change in $\tau_{\rm SF}$ by a factor of 2 makes a similar 0.5 magnitude change of the simulated luminosity functions, but the effect is still substantially sub-linear. Finally, since the two parameters have

[5] The exact values of redshifts are matched to Hubble filters used in observations: $z = 5.0, 5.9, 6.8, 8.0, 9.0, 10.0$

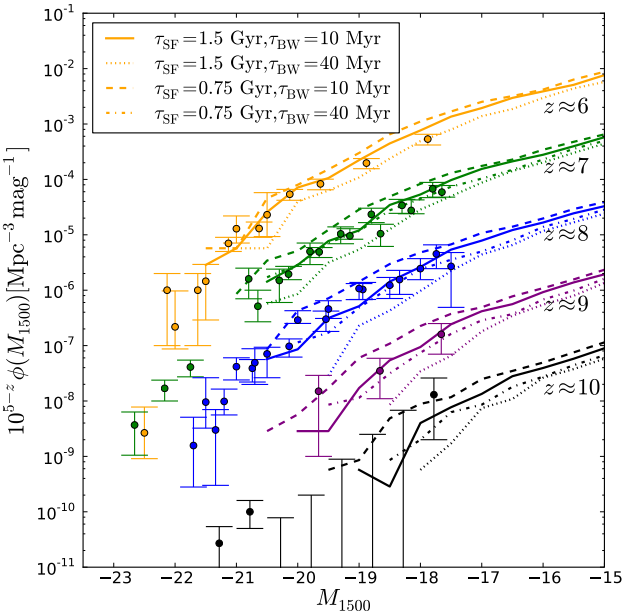

FIG. 2.— Ultraviolet galaxy luminosity functions for simulation sets with varied parameters of the star formation model. The time-scale for delayed cooling τ_{BW} and the depletion time τ_{SF} (i.e. star formation efficiency) do affect the computed luminosity functions, but *not* a directly proportional way due to well-known self-regulation of star formation.

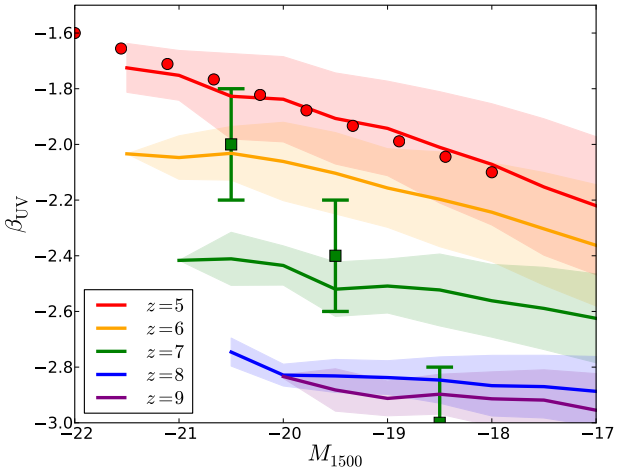

FIG. 3.— Ultraviolet continuum slopes of galactic SEDs for our simulated galaxies as a function of UV luminosity (average - lines, rms - shaded). Red circles show the observational constraints at $z = 5$ from Rogers et al. (2013), while green squares with error-bars are $z = 7$ measurements from Bouwens et al. (2010). We do not match the $z = 7$ slope gradient, and the reason for the discrepancy is currently unclear.

opposite effects, a higher star formation efficiency (lower τ_{SF}) can always be compensated by a stronger feedback (longer τ_{BW}), as is illustrated by the set B20.sf2.uv2.bw40. That result should not be surprising at all - it is well established that stellar feedback "self-regulates" star formation on kiloparsec scales (Schaye et al. 2009; Agertz et al. 2011; Hopkins et al. 2011; Agertz et al. 2013b; Hopkins et al. 2013). The sensitivity of our star formation model to numerical parameters is somewhat higher than is usually found at lower redshifts, reflecting the fact that complete self-regulation takes some time to get established; that is also consistent with prior work (e.g. Schaye et al. 2009; Agertz et al. 2011).

Another observational constraint on our star formation model is offered by the observed UV continuum slopes of high redshift galaxies. To measure the UV continuum slopes of model galaxies we compute the monochromatic fluxes at 1300Å, 1400Å, 1500Å, 1600Å, and 1700Å for our fiducial B20.sf1.uv2.bw10 set[6], and fit a power-law relation $F_\lambda \propto \lambda^\beta$ using a simple least-squares fit in a log-log plane. In Figure 3 we show the average UV continuum slopes measured from our simulations and the rms scatter around them, as well as observational measurements at $z = 5$ and $z = 7$. Our simulations match the observed slopes at $z = 5$ rather well, but do not reproduce the trend of bluer spectra of fainter galaxies at $z = 7$.

The latter discrepancy is somewhat surprising, since by matching the whole evolution of luminosity functions, our simulations reproduce not only star formation rates at $z = 7$, but the whole prior star formation histories of galaxies. Nevertheless, it is possible to come up with several potential reasons for the discrepancy: our dust obscuration model (Appendix B) may be over-simplistic, the FSPS code may not be sufficiently accurate, as may be observational, broad-band based diagnostics for the true spectral slope; finally, we may be lacking numerical resolution or the stellar feedback model may be too crude to capture the variability of star formation in the smallest galaxies. For all these reasons, we leave resolving this apparent discrepancy to future work.

[6] Such calculations would be too computationally expensive for all of B40.sf1.uv1.bw10 simulations, and are not really needed.

4.2. *Ionizing Emissivity*

Our star formation model, specified by parameters τ_{SF} and τ_{BW}, appears to work reasonably well. The last remaining parameter in the simulations that needs to be calibrated is the escape fraction up to the simulation resolution limit ϵ_{UV}. This parameter can be calibrated with the observed spectra of high-redshift quasars - ionizing emissivity of our sources is proportional to ϵ_{UV}, and, therefore, the whole process of reionization and its aftermath - the Lyα forest at $z = 5 - 6$ - is affected by ϵ_{UV}.

In order to model absorption spectra of high-redshift quasars, we compute synthetic Lyα spectra along 1000 totally random lines of sight at several simulation snapshots. Since simulations use periodic boundary conditions, we extend each line of sight to twice the simulation box size - random lines of sight in a periodic universe are only weakly affected by the artificial periodicity if they do not extend beyond twice the box length. For the $20h^{-1}$ Mpc box that corresponds to about $\Delta z = 0.15$ at $z = 6$, which is a typical redshift resolution for averaging properties of Lyα spectra in observed spectra (Fan et al. 2006b).

In Figure 4 we show the evolution of the mean Gunn-Peterson optical depth and the volume weighted mean HI fraction in four of our simulation sets: three $20h^{-1}$ Mpc boxes with $\epsilon_{UV} = 0.1$, 0.2, and 0.4, and our fiducial $40h^{-1}$ Mpc box. There are several conclusions that can be drawn from that figure.

Firstly, changing ionizing emissivity by a factor of 2 changes the moment of overlap of ionizing bubbles, indicated by the sharp drop in volume weighted mean HI fraction (Gnedin 2000, 2004; Gnedin & Fan 2006), by about $\Delta z \approx 0.5$.

Secondly, the opacity of the post-reionization Lyα forest are best matched by $\epsilon_{UV} = 0.2$ value independently of the box size.

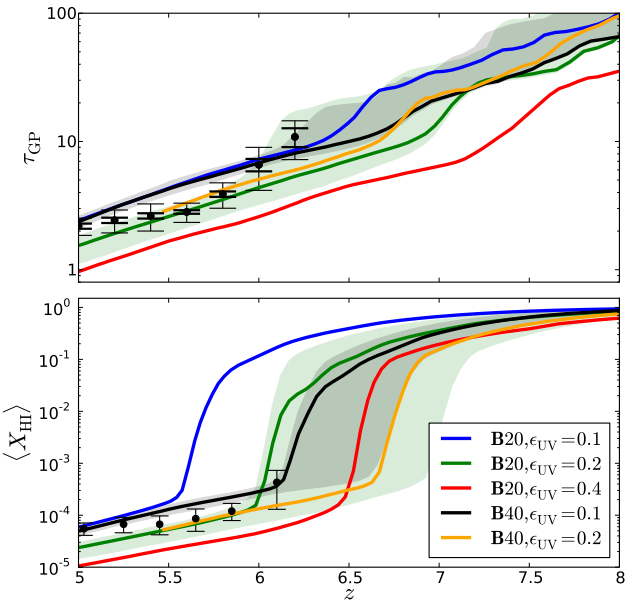

FIG. 4.— Gunn-Peterson optical depth (top) and volume-weighted HI fraction (bottom) vs redshift for four simulation sets: B20.sf1.uv1.bw10 (blue), B20.sf1.uv2.bw10 (green), B20.sf1.uv4.bw10 (red), and B40.sf1.uv1.bw10 (black). Solid lines show the average quantities, while the shaded regions for fiducial sets B20.sf1.uv2.bw10 and B40.sf1.uv1.bw10 span the limits of variation among 6/3 independent realizations. Data points are from Fan et al. (2006b).

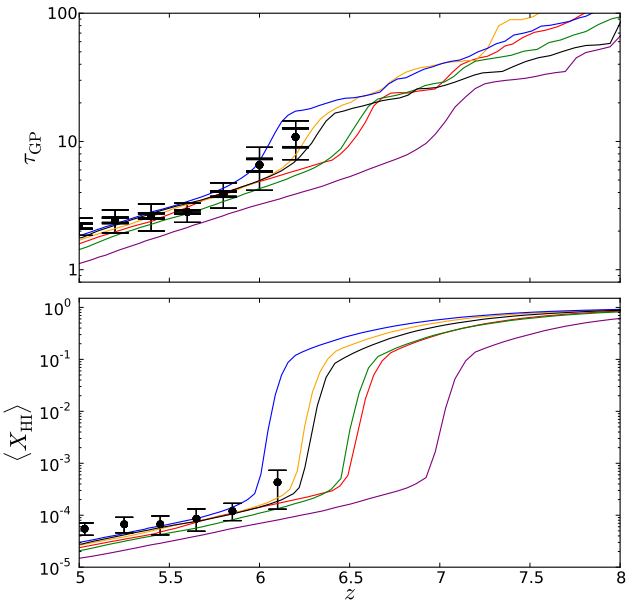

FIG. 5.— Average Gunn-Peterson optical depth (top) and volume-weighted HI fraction (bottom) vs redshift for 6 independent realizations of the fiducial set B20.sf1.uv2.bw10. Data points are from Fan et al. (2006b).

Thirdly, and most importantly, we do not yet reach numerical convergence at the box size of $40h^{-1}$ Mpc - the fact that out fiducial sets B20.sf1.uv2.bw10 and B40.sf1.uv1.bw10 have different values of the ϵ_{UV} parameter, but similar reionization histories, indicates that even 3 independent realizations of a $40h^{-1}$ Mpc are not enough to obtain an accurate prediction for the mean Gunn-Peterson optical depth or the volume weighted mean neutral fraction.

Finally, our simulations do not match the observational points at $z \gtrsim 6$ particularly well. However, we do not consider that a serious problem exactly for the third reason above: our sets of simulation boxes sample the Lyα forest at each redshift interval way better than the observational measurements, and yet they are still far from convergence. Hence, the observational values are not the converged results either, and the discrepancy between the observational constraints and our simulations does not necessarily imply a major failure of our physical model, but may also be due to just cosmic variance.

Large cosmic variance is further illustrated in Figure 5, where we show the average Gunn-Peterson optical depth and the volume weighted mean HI fraction for all 6 independent realization of our fiducial B20.sf1.uv2.bw10 set. As one can see, the variations from realization to realization are very large (recall, that the $20h^{-1}$ Mpc box is well-matched to the redshift bin of observational measurement of $\Delta z \approx 0.15$), and two of our realizations go through the observational points reasonably well.

The reason for such a large sensitivity to cosmic variance is in the extreme non-linearity of the relationship between the Gunn-Peterson optical depth τ_{GP} and the gas density, which makes τ_{GP} extremely sensitive to outlayers. For example, consider N lines of sight at some redshift during reionization, of which only one has non-zero transmitted flux F_1. The average flux over N lines is F_1/N, and the corresponding Gunn-Peterson optical depth is

$$\tau_{GP} = -\ln(F_1/N) = \tau_1 + \ln N,$$

where τ_1 is the Gunn-Peterson optical depth along that one line of sight with partial absorption. In observations, typically only a few lines of sight contribute to a given redshift bin, i.e. $N = 3 - 5$. Hence, a single line of sight with $\tau_1 = 10$ (an observational value at $z = 6.2$) results in the measured "average" of $\tau_{GP} \approx 11.1 - 11.6$, only slightly above τ_1.

Based on this reasoning, we use only post-reionization Lyα data ($z < 6$) for calibrating our simulations, and rely on the derived volume-weighted mean HI fraction from Fan et al. (2006b) as preferred calibration data, even if the Gunn-Peterson optical depth is a directly observed quantity - $\langle X_{HI} \rangle_V$ is, effectively, a convolution over the whole distribution function of observed Lyα fluxes in individual spectral pixels, just like τ_{GP}, but it is more sensitive to typical values of the transmitted flux, while τ_{GP} is heavily weighted towards the tail of the distribution. In that sense it is a less biased, even if less direct, observational probe.

Hence, our preferred value for the parameter ϵ_{UV} is between 0.1 and 0.2 (with 0.2 matching observations better); the computational expense of simulations (and lack of convergence between $20h^{-1}$ Mpc and $40h^{-1}$ Mpc boxes) prevents us from actually fitting for the value of ϵ_{UV} to higher precision.

5. CONCLUSIONS

Cosmic Reionization On Computers (CROC) project is a long-term simulation campaign for modeling the process of cosmic reionization in sufficiently large simulations volumes (above 100 Mpc) with detailed physical modeling and spatial resolution better than 0.5 kpc (simulation cell size of less than 150 pc).

A simple model of star formation and feedback, based on the linear Kennicutt-Schmidt relation in the molecular gas and a widely used "delayed cooling" or "blastwave" feedback, is able to reproduce the observed galaxy UV luminosity func-

tions in the whole redshift range $z = 6 - 10$ with a value for the molecular gas depletion time of $\tau_{\rm SF} = 1.5\,{\rm Gyr}$, consistent with observations at $z \sim 0$ and $z = 1 - 2$.

A reasonable choice for the $\epsilon_{\rm UV}$ parameter, a quantity that describes photon losses on scales unresolved in our simulations, of $\epsilon_{\rm UV} = 0.1 - 0.2$ results in reionization history that is reasonably consistent with the observed opacity of the Lyα forest in the spectra of SDSS quasars at $z < 6$. An even better consistency can be achieved by fitting the simulations to the data, albeit at (presently unrealistically) large computational expense.

The observed increase in the Gunn-Peterson optical depth at $z > 6$ (Fan et al. 2006b) has been interpreted by several groups (including ours) as evidence for the reionization overlap (Becker et al. 2001; White et al. 2003; Gnedin 2004; Fan et al. 2006a; Gnedin & Fan 2006). That increase is, however, a subject to large cosmic variance; with 6 independent realizations, each corresponding to multiple lines of sight, we find a spread in the redshift of overlap of about $\Delta z \approx 1$. Since the observational constraints have even less statistical power than our simulations, they have not yet converged on the true evolution of the average Gunn-Peterson optical depth, and may, therefore, be significantly biased.

We are grateful to Andrea Ferrara and Matthew McQuinn for valuable comments and suggestions that significantly improved the original manuscript.

Simulations used in this work have been performed on the Joint Fermilab - KICP cluster "Fulla" at Fermilab, on the University of Chicago Research Computing Center cluster "Midway", and on National Energy Research Supercomputing Center (NERSC) supercomputers "Hopper" and "Edison".

APPENDIX

MODEL FOR QUASAR SOURCES

For the intrinsic quasar SED we use our own fit to the Richards et al. (2006) model,

$$\nu L_\nu \propto \frac{9.5\times10^{-5}}{(1+(h\nu/300\,{\rm eV}))^{0.8}} e^{-h\nu/500\,{\rm keV}} + 0.1\frac{(10\,{\rm eV}/h\nu)^{2.2}}{\left(1+(9\,{\rm eV}/h\nu)^5\right)^{0.4}} + 5.8e^{-h\nu/0.2\,{\rm eV}}.$$

The evolution of the bolometric quasar luminosity function has been determined by Hopkins et al. (2007). We fit the quasar bolometric luminosity density as a function of redshift as

$$L_{\rm QSO}(z) = 10^{7.7}\frac{{\rm L}_\odot}{{\rm Mpc}^3}\left(\left[e^{1.2(z-4)}\right]^{1/3} + \left[3e^{-2.7z}\right]^{1/3}\right)^{-3},$$

and we use a k-correction of $k_{\rm ion} = 3.9$ to translate from the bolometric to ionizing quasar luminosity.

DUST OBSCURATION MODEL

In this work we adopt a simple, but reasonable dust obscuration model for our simulated galaxies, in which the dust optical depth at wavelength λ is estimated as

$$\tau_\lambda = \sigma_D(\lambda) Z_* N_{\rm eff}, \tag{B1}$$

where $N_{\rm eff}$ is a parameter to be calibrated from the observational data, Z_* is the stellar metallicity in solar units, and $\sigma_D(\lambda)$ is the dust cross-section at solar metallicity. For the specific extinction law, we take the SMC dust (Weingartner & Draine 2001), since most of our simulated galaxies at $z = 5 - 6$ have metallicities similar to SMC, and normalize it to solar metallicity by assuming the SMC metallicity of -0.7 dex (see Gnedin et al. 2008, for details),

$$\sigma_D(\lambda) = 1.76\times10^{-21}\,{\rm cm}^2\left(\frac{1500\text{Å}}{\lambda}\right)^{1.1}.$$

Figure 6 shows the observational constraints on the dust abundance in $z = 5$ and $z = 6$ galaxies from Bouwens et al. (2009). Our simple dust obscuration model can roughly match these constraints with the value of $N_{\rm eff} \approx 5\times10^{21}\,{\rm cm}^{-2}$. At $z > 7$ the observational constraints are consistent with no dust obscuration (Bouwens et al. 2009, 2011); to account for that we adopt an extremely crude but simple ansatz for $N_{\rm eff}$:

$$N_{\rm eff} = 5\times10^{21}\,{\rm cm}^{-2}\min\left(1, \max\left(0, 0.5(8-z)\right)\right)$$

($N_{\rm eff} = 5\times10^{21}\,{\rm cm}^{-2}$ for $z \le 6$, $N_{\rm eff} = 0$ for $z \ge 8$, and is linearly interpolated in between to avoid discontinuities). With that ansatz the dust obscuration at $z = 7$ is not identically zero, but is small enough to be unimportant and undetectable observationally.

OPTICALLY THIN VARIABLE EDDINGTON TENSOR APPROXIMATION IN THE ART CODE

Two-field Ansatz for the Radiation Field

Consider a radiative transfer equation in the expanding universe, in comoving reference frame,

$$\frac{a}{c}\frac{\partial J_\nu}{\partial t} + \vec{n}\frac{\partial J_\nu}{\partial \vec{x}} - \frac{aH}{c}\left(\nu\frac{\partial J_\nu}{\partial \nu} - 3J_\nu\right) = -k_\nu J_\nu + S_\nu, \tag{C1}$$

where $J_\nu(t, \vec{x}, \vec{n})$ is the radiation specific intensity, k_ν is the absorption coefficient (per unit comoving distance), and S_ν is the source function (in appropriate units).

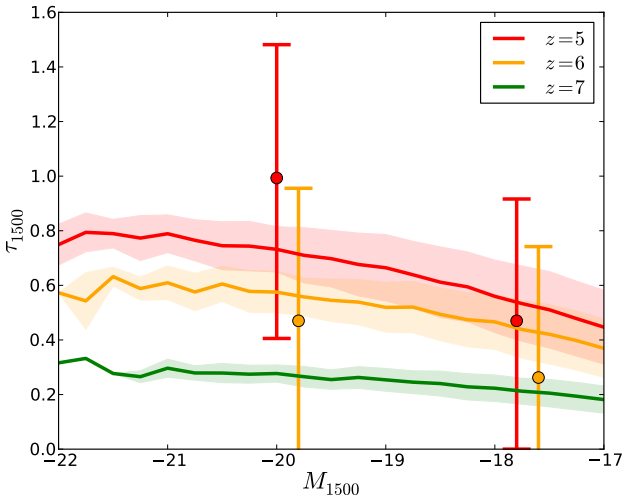

FIG. 6.— Dust optical depth at λ = 1500Å vs galaxy AB magnitude at the same wavelength. Points with error-bars are the observational constraints from Bouwens et al. (2009), while lines with bands are a combination of simulation sets B20.sf1.uv2.bw10 and B40.sf1.uv1.bw10. Different colors correspond to redshifts in the rainbow order.

In the following, it is assumed that

A1 all sources have the same spectral shape, i.e. the frequency dependence of S_ν can be factored out, and that

A2 sources are isotropic (S_ν does not depend on $\vec{n}$).

Both these assumptions can be relaxed, if necessary.

With these assumptions, we can write

$$S_\nu(t, \vec{x}) = L_\nu \rho_S(t, \vec{x}).$$

For example, for stellar sources, $\rho_S(t, \vec{x})$ can be the mass density of massive stars.

In cosmological simulations, it is convenient to replace specific intensity J_ν with two separate functions, f_ν and g_ν, as follows:

$$J_\nu = \bar{J}_\nu f_\nu + L_\nu(g_\nu - \bar{g}_\nu f_\nu), \tag{C2}$$

where $\bar{J}_\nu$ is the spatially and angle averaged specific intensity (i.e. cosmic background), which satisfies the following equation,

$$\frac{a}{c}\frac{\partial \bar{J}_\nu}{\partial t} - \frac{aH}{c}\left(\nu\frac{\partial \bar{J}_\nu}{\partial \nu} - 3\bar{J}_\nu\right) = -\bar{k}_\nu \bar{J}_\nu + \bar{S}_\nu,$$

where we defined the mean absorption coefficient as radiation-field-weighted,

$$\bar{k}_\nu \equiv \frac{\langle k_\nu J_\nu \rangle}{\bar{J}_\nu}.$$

Analogously, $\bar{g}_\nu$ is the spatially and angle averaged g_ν.

The reason to impose such an ansatz is to simplify the frequency dependence of the radiation field - in principle, one would need to follow several hundred radiation fields, one for each frequency bins, in order to compute accurately most of ionization and other chemical rates. This is not practical, obviously. Hence, the goal of ansatz (C2) is to concentrate most of the frequency dependence in the pre-factors, and hope that both f_ν and g_ν depend on the frequency only moderately.

For example, one can imagine that the radiation field shining on a particular place in space is a combination of a contribution of the cosmic background (perhaps, attenuated by additional local absorption) and the radiation from nearby sources (perhaps, also attenuated by additional local absorption). In that case f_ν and g_ν would only have to account for the local absorption, and in places where the local absorption is negligible, would become completely frequency independent.

The specific form of this ansatz is dictated by the need to satisfy the consistency condition, since J_ν now depends on its own average; averaging both sides of Equation (C2) over space and angles gives

$$\bar{J}_\nu = \bar{J}_\nu \bar{f}_\nu + L_\nu(\bar{g}_\nu - \bar{g}_\nu \bar{f}_\nu),$$

which can be satisfied if $\bar{f}_\nu = 1$.

There are more than one way to introduce the ansatz similar to Equation (C2). That particular form, however, ensures that both f_ν and g_ν remain always non-negative, which is a desirable property for a numerical implementation (as it avoids numerical loss of precision).

Equation (C2) is nothing more than an ansatz, we replaced one unknown function with two, hence we can impose a condition on these two functions. The condition we impose is that terms with f_ν and g_ν cancel out separately. In the following we drop the frequency subscripts for brevity, all quantities except ρ_S remain functions of frequency. In addition, we adopt a Newtonian

approximation for f and g, omitting terms with the Hubble parameter for them, but retaining cosmological terms for $\bar{J}_\nu$ (see Gnedin & Abel 2001, for more detailed description of this approximation). With these simplifications, one obtains

$$f\left[-\bar{k}\bar{J}+\bar{S}\right]-Lf\frac{a}{c}\frac{\partial\bar{g}}{\partial t}+(\bar{J}-L\bar{g})\frac{Df}{dl}+L\frac{Dg}{dl}=$$
$$=-(\bar{J}-L\bar{g})kf-Lkg+L\rho_S\,, \tag{C3}$$

where we use a shorthand

$$\frac{D}{dl}\equiv\frac{a}{c}\frac{\partial}{\partial t}+\vec{n}\frac{\partial}{\partial\vec{x}}$$

for the derivative along the light cone.

The condition we impose is then

$$\frac{Dg}{dl}=-kg+\rho_S\,, \tag{C4}$$

which, in Newtonian limit (ignoring terms with $1/c$) has a simple solution,

$$g(t,\vec{x},\vec{n})=\int_0^\infty dl\,\rho_S(t,\vec{x}+\vec{n}l)e^{-\tau(\vec{x},\vec{x}+\vec{n}l)}, \tag{C5}$$

where $\tau(\vec{x}_1,\vec{x}_2)$ is the optical depth between points $\vec{x}_1$ and $\vec{x}_2$,

$$\tau(\vec{x}_1,\vec{x}_2)=|\vec{x}_1-\vec{x}_2|\int_0^1 ds\,k\left(\vec{x}_1+s(\vec{x}_1-\vec{x}_2)\right).$$

An even more familiar form is the angle average of g,

$$\langle g\rangle(t,\vec{x})=\frac{1}{4\pi}\int d^3x'\,\frac{\rho_S(\vec{x'})}{(\vec{x}-\vec{x'})^2}e^{-\tau(\vec{x},\vec{x'})},$$

which is simply an integral of $\rho_S/(4\pi r^2)$ over all sources, diminished by the opacity between the source and the current location. In particular, g is manifestly positive everywhere in the computational domain.

Using Equation (C4) in (C3), we find

$$(\bar{J}-L\bar{g})\left[\frac{Df}{dl}+kf\right]=f\left[\bar{k}\bar{J}-L\bar{\rho_S}\right]+Lf\frac{a}{c}\frac{\partial\bar{g}}{\partial t}.$$

Averaging Equation (C4) over space and angle results in

$$\frac{a}{c}\frac{\partial\bar{g}}{\partial t}=-\langle kg\rangle+\bar{\rho_S}\,.$$

Combining the last two equations together, we find

$$(\bar{J}-L\bar{g})\left[\frac{Df}{dl}+kf\right]=f\left[\bar{k}\bar{J}-L\langle kg\rangle\right]. \tag{C6}$$

Finally, we can use Equation (C2) to compute the average absorption,

$$\bar{k}\bar{J}\equiv\langle kJ\rangle=(\bar{J}-L\bar{g})\langle kf\rangle+L\langle kg\rangle.$$

Substituting $\langle kg\rangle$ from the above equation into Equation (C6), we obtain the final equation for the function f,

$$\frac{Df}{dl}=-kf+f\langle kf\rangle. \tag{C7}$$

Equations (C4) and (C7) are our master equations for the cosmological radiative transfer. At this point no approximations have been made except for the assumptions A1 and A2 above.

One undesirable property of Equation (C7) is that it numerically unstable. To see that, we can average it over space and angle,

$$\frac{a}{c}\frac{\partial\bar{f}}{\partial t}=\langle kf\rangle(\bar{f}-1). \tag{C8}$$

Value $\bar{f}=1$ is indeed a solution of this equation, but an unstable one: $\frac{\partial\bar{f}}{\partial t}>0$ for $\bar{f}>1$ and $\frac{\partial\bar{f}}{\partial t}<0$ for $\bar{f}<1$. To circumvent this problem, we multiply the last term in equation (C7) by a function $q(\bar{f})$,

$$\frac{Df}{dl}=-kf+q(\bar{f})f\langle kf\rangle, \tag{C9}$$

where $q(1)=1$. It is easy to show that, if $q'(1)<-1$, then Equation (C9) is numerically stable.

A fiducial choice for q is

$$q(x) = \frac{2}{x} - 1,$$

but, in the future, other forms for that function need to be explored.

OTVET Approximation in the Two-field Ansatz

In Gnedin & Abel (2001) it is shown how to derive a single diffusion-like equation for the angle average of fields f and g. Namely, if

$$F_\nu(t, \vec{x}) \equiv \frac{1}{4\pi} \int d\Omega f_\nu(t, \vec{x}, \vec{n}),$$
$$G_\nu(t, \vec{x}) \equiv \frac{1}{4\pi} \int d\Omega g_\nu(t, \vec{x}, \vec{n}),$$

then (again omitting the frequency dependence for brevity)

$$\frac{\partial G}{\partial \xi} = \frac{\partial}{\partial x^j}\left(\frac{1}{k}\frac{\partial G h_G^{ij}}{\partial x^i}\right) - kG + \rho_S, \tag{C10}$$

$$\frac{\partial F}{\partial \xi} = \frac{\partial}{\partial x^j}\left(\frac{1}{k}\frac{\partial F h_F^{ij}}{\partial x^i}\right) - kF + q(\bar{F})F\langle kF\rangle, \tag{C11}$$

where $d\xi = \hat{c}\, dt/(2a)$, $\hat{c} \le c$ is the "reduced speed of light" (Gnedin & Abel 2001), and averaging in Equation (C11) is done over the space (obviously, $\bar{f} = \bar{F}$).

We choose Eddington tensors differently in Equations (C10) and (C11): for a cosmological simulation in a periodic box, h_G^{ij} is chosen as the optically thin Eddington tensor from all sources inside a periodic box, while the Eddington tensor for the background radiation is taken to be isotropic, $h_F^{ij} = \delta^{ij}/3$.

Elliptic Solver for OTVET Diffusion-like Equation

Consider OTVET-type equation for some function $E(\xi, \vec{x})$ and some tensor $h^{ij}(\xi, \vec{x})$,

$$\frac{\partial E}{\partial \xi} = \frac{\partial}{\partial x^j}\left(\frac{1}{k}\frac{\partial E h^{ij}}{\partial x^i}\right) - kE + s, \tag{C12}$$

where $k(\xi, \vec{x})$ is the absorption coefficient and $s(\xi, \vec{x})$ is the source term. This equation is discretized in some fashion in space on a set of indicies $\{I\}$, where I may may an SPH particle number, a set of indicies (i, j, k) on a regular mesh, or any other discretization. We assume that the discretization is such that all quantities E_I, h_I^{ij}, k_I, and s_I are co-located in space on the same set of resolution elements $\{I\}$.

The discretization scheme is associated with a spatial scale Δx (cell size on a regular mesh, SPH kernel size, etc). Each cycle of the OTVET solver (for example, a time-step of a hydro scheme) consists of the set of consecutive iterations, which we label as $E_I^{(n)}$, where $n = 0, 1, 2, ...$

The second-order term in Equation (C12) is discretized as

$$\left.\frac{\partial}{\partial x^j}\left(\frac{1}{k}\frac{\partial E h^{ij}}{\partial x^i}\right)\right|_I \approx \frac{1}{\Delta x}\hat{\mathcal{D}}_I[E; a],$$

where $a_I \equiv k_I \Delta x$ is the dimensionless absorption coefficient and $\hat{\mathcal{D}}_I[E; a]$ is a linear operator on the set of all values E_I,

$$\hat{\mathcal{D}}_I[E; a] = \sum_J w_{I,J} E_J,$$

with the sum being over all indicies J. Dimensionless weights $w_{I,J}$ depend on various a_I as appropriate, and most of $w_{I,J}$ are zero because the second order term only has a finite support.

For example, for a regular mesh with $I = (i, j, k)$,

$$\hat{\mathcal{D}}_I[E; a] = \frac{U^x_{i+1,j,k} - U^x_{i,j,k}}{a_{i+1/2,j,k}} + \frac{U^x_{i-1,j,k} - U^x_{i,j,k}}{a_{i-1/2,j,k}} + \frac{U^y_{i,j+1,k} - U^y_{i,j,k}}{a_{i,j+1/2,k}} + \frac{U^y_{i,j-1,k} - U^y_{i,j,k}}{a_{i,j-1/2,k}} + \frac{U^z_{i,j,k+1} - U^z_{i,j,k}}{a_{i,j,k+1/2}} + \frac{U^z_{i,j,k-1} - U^z_{i,j,k}}{a_{i,j,k-1/2}},$$

where $a_{i+1/2,j,k} = (a_{i,j,k} + a_{i+1,j,k})/2 + \epsilon$, etc, and a small offset $\epsilon = 10^{-3}$ is added to avoid division by zero (we have verified it

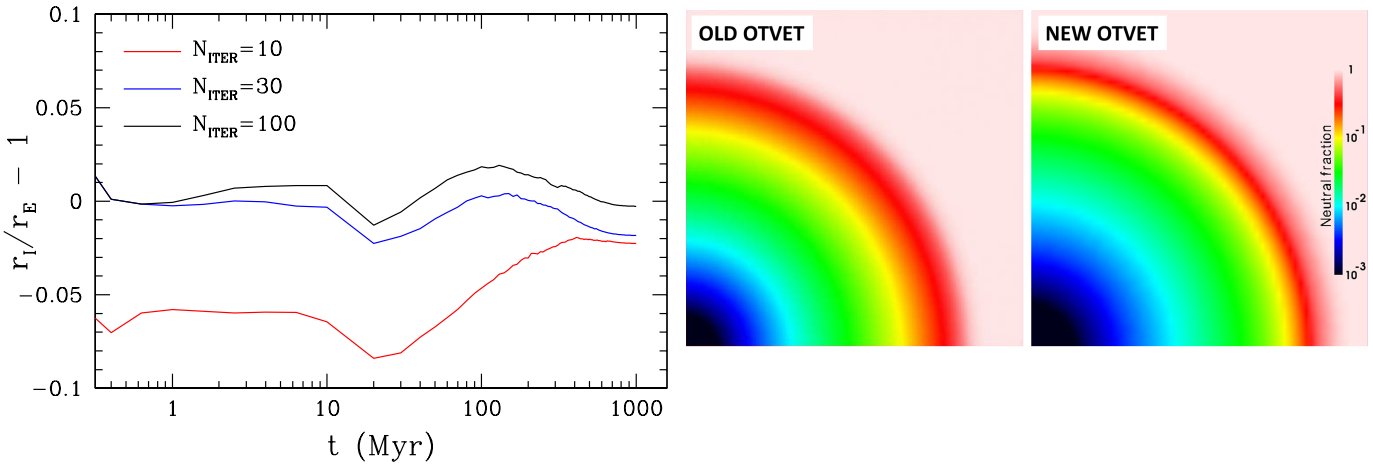

FIG. 7.— Left: Error in the position of the ionization front r_I as a function of time in the Iliev et al. (2006a) Test # 1 for several numbers of iterations (as indicated on the legend). About 30 iterations are sufficient to achieve the convergence. Right: Comparison of the old and new OTVET implementations in Test 1 of Iliev et al. (2006a). In the new implementation the I-front is sharper and it location is more accurate. This images are to be compared with Figure 6 of Iliev et al. (2006a).

makes no effect on the actual solution). Fluxes U^j are defined as

$$U^x_{i,j,k} = E_{i,j,k} h^{xx}_{i,j,k} + \frac{1}{4}\left(E_{i,j+1,k} h^{xy}_{i,j+1,k} + E_{i,j-1,k} h^{xy}_{i,j-1,k} + E_{i,j,k+1} h^{xz}_{i,j,k+1} + E_{i,j,k-1} h^{xz}_{i,j,k-1}\right),$$
$$U^y_{i,j,k} = E_{i,j,k} h^{yy}_{i,j,k} + \frac{1}{4}\left(E_{i+1,j,k} h^{yx}_{i+1,j,k} + E_{i-1,j,k} h^{yx}_{i-1,j,k} + E_{i,j,k+1} h^{yz}_{i,j,k+1} + E_{i,j,k-1} h^{yz}_{i,j,k-1}\right),$$
$$U^z_{i,j,k} = E_{i,j,k} h^{zz}_{i,j,k} + \frac{1}{4}\left(E_{i+1,j,k} h^{zx}_{i+1,j,k} + E_{i-1,j,k} h^{zx}_{i-1,j,k} + E_{i,j+1,k} h^{zy}_{i,j+1,k} + E_{i,j-1,k} h^{zy}_{i,j-1,k}\right),$$

etc.

Let us define two new, iteration-independent, discretized quantities,

$$A_I \equiv \frac{\gamma}{1 + \gamma\left(\beta a_I - w_{I,I}\right)}$$

($w_{I,I} < 0$ is the diagonal term of the operator $\hat{\mathcal{D}}_I[E; a]$) and

$$B_I \equiv s_I \Delta x - (1-\beta) a_I E_I^{(0)},$$

where α, β, and γ are constants.

Then one iteration of the OTVET elliptic solver consists of computing

$$d_I^{(n)} = \hat{\mathcal{D}}_I[E^n; a] - \beta a_I E_i^n + B_I,$$

for all I, followed by updating E_I as

$$E_I^{(n+1)} = E_I^{(n)} + \alpha A_I d_I^{(n)}.$$

Numerical stability requires $\alpha < 1$. A set of values that works particularly well is

$$\begin{aligned} \alpha &= 0.8, \\ \beta &= 0.1, \\ \gamma &= 1. \end{aligned}$$

The left panel of Figure 7 shows the error in the propagation of the ionization front as a function of time in the Test #1 of Iliev et al. (2006a). This is the most sensitive to the iteration count of all tests presented in Iliev et al. (2006a) and Iliev et al. (2009). As one can see, about 30 iterations are sufficient to achieve 2% precision in the ionization front evolution, and mere 10 iterations already give 5% precision. The right panel of the same figure shows the improvement in tracking the ionization front with the new scheme. It should be compared with Figure 6 of Iliev et al. (2006a) - now the quality of OTVET solution approaches that of the best ray-tracing schemes.

REFERENCES

Agertz, O., Kravtsov, A. V., Leitner, S. N., & Gnedin, N. Y. 2013a, ApJ, 770, 25
—. 2013b, ApJ, 770, 25
Agertz, O., Teyssier, R., & Moore, B. 2011, MNRAS, 410, 1391
Alvarez, M. A. & Abel, T. 2007, MNRAS, 380, L30
—. 2012, ApJ, 747, 126
Battaglia, N., Trac, H., Cen, R., & Loeb, A. 2013, ApJ, 776, 81

Becker, R. H., Fan, X., White, R. L., Strauss, M. A., Narayanan, V. K., Lupton, R. H., Gunn, J. E., Annis, J., Bahcall, N. A., Brinkmann, J., Connolly, A. J., Csabai, I., Czarapata, P. C., Doi, M., Heckman, T. M., Hennessy, G. S., Ivezić, Ž., Knapp, G. R., Lamb, D. Q., McKay, T. A., Munn, J. A., Nash, T., Nichol, R., Pier, J. R., Richards, G. T., Schneider, D. P., Stoughton, C., Szalay, A. S., Thakar, A. R., & York, D. G. 2001, AJ, 122, 2850

Bigiel, F., Leroy, A., Walter, F., Brinks, E., de Blok, W. J. G., Madore, B., & Thornley, M. D. 2008, AJ, 136, 2846

Bigiel, F., Leroy, A. K., Walter, F., Brinks, E., de Blok, W. J. G., Kramer, C., Rix, H. W., Schruba, A., Schuster, K., Usero, A., & Wiesemeyer, H. W. 2011, ApJ, 730, L13+

Bolatto, A. D., Leroy, A. K., Jameson, K., Ostriker, E., Gordon, K., Lawton, B., Stanimirovic, S., Israel, F. P., Madden, S. C., Hony, S., Sandstrom, K. M., Bot, C., Rubio, M., Winkler, P. F., Roman-Duval, J., van Loon, J. T., Oliveira, J. M., & Indebetouw, R. 2011, ArXiv e-prints

Bouwens, R. J., Illingworth, G. D., Franx, M., Chary, R.-R., Meurer, G. R., Conselice, C. J., Ford, H., Giavalisco, M., & van Dokkum, P. 2009, ApJ, 705, 936

Bouwens, R. J., Illingworth, G. D., Franx, M., & Ford, H. 2007, ApJ, 670, 928

Bouwens, R. J., Illingworth, G. D., Oesch, P. A., Labbé, I., Trenti, M., van Dokkum, P., Franx, M., Stiavelli, M., Carollo, C. M., Magee, D., & Gonzalez, V. 2011, ApJ, 737, 90

Bouwens, R. J., Illingworth, G. D., Oesch, P. A., Trenti, M., Stiavelli, M., Carollo, C. M., Franx, M., van Dokkum, P. G., Labbé, I., & Magee, D. 2010, ApJ, 708, L69

Bowler, R. A. A., Dunlop, J. S., McLure, R. J., Rogers, A. B., McCracken, H. J., Milvang-Jensen, B., Furusawa, H., Fynbo, J. P. U., Taniguchi, Y., Afonso, J., Bremer, M. N., & Le Fevre, O. 2013, ArXiv e-prints

Bradley, L. D., Trenti, M., Oesch, P. A., Stiavelli, M., Treu, T., Bouwens, R. J., Shull, J. M., Holwerda, B. W., & Pirzkal, N. 2012, ApJ, 760, 108

Brook, C. B., Stinson, G. S., Gibson, B. K., Kawata, D., House, E. L., Miranda, M. S., Macciò, A. V., Pilkington, K., Roškar, R., Wadsley, J., & Quinn, T. R. 2012, MNRAS, 426, 690

Choudhury, T. R. & Ferrara, A. 2005, MNRAS, 361, 577

—. 2006, MNRAS, 371, L55

Conroy, C. & Gunn, J. E. 2010, ApJ, 712, 833

Conroy, C., White, M., & Gunn, J. E. 2010, ApJ, 708, 58

Daddi, E., Bournaud, F., Walter, F., Dannerbauer, H., Carilli, C. L., Dickinson, M., Elbaz, D., Morrison, G. E., Riechers, D., Onodera, M., Salmi, F., Krips, M., & Stern, D. 2010, ApJ, 713, 686

Fan, X., Carilli, C. L., & Keating, B. 2006a, ARA&A, 44, 415

Fan, X., Strauss, M. A., Becker, R. H., White, R. L., Gunn, J. E., Knapp, G. R., Richards, G. T., Schneider, D. P., Brinkmann, J., & Fukugita, M. 2006b, AJ, 132, 117

Furlanetto, S. R., Hernquist, L., & Zaldarriaga, M. 2004, MNRAS, 354, 695

Furlanetto, S. R., McQuinn, M., & Hernquist, L. 2006, MNRAS, 365, 115

Furlanetto, S. R. & Oh, S. P. 2005, MNRAS, 363, 1031

Genzel, R., Tacconi, L. J., Gracia-Carpio, J., Sternberg, A., Cooper, M. C., Shapiro, K., Bolatto, A., Bouché, N., Bournaud, F., Burkert, A., Combes, F., Comerford, J., Cox, P., Davis, M., Schreiber, N. M. F., Garcia-Burillo, S., Lutz, D., Naab, T., Neri, R., Omont, A., Shapley, A., & Weiner, B. 2010, MNRAS, 407, 2091

Gnedin, N. Y. 2000, ApJ, 535, 530

—. 2004, ApJ, 610, 9

Gnedin, N. Y. & Abel, T. 2001, New Astronomy, 6, 437

Gnedin, N. Y. & Fan, X. 2006, ApJ, 648, 1

Gnedin, N. Y. & Hollon, N. 2012, ApJS, 202, 13

Gnedin, N. Y. & Kravtsov, A. V. 2011, ApJ, 728, 88

Gnedin, N. Y., Kravtsov, A. V., & Chen, H.-W. 2008, ApJ, 672, 765

Gnedin, N. Y., Kravtsov, A. V., & Rudd, D. H. 2011, ApJS, 194, 46

Gnedin, N. Y. & Ostriker, J. P. 1997, ApJ, 486, 581

Governato, F., Brook, C., Mayer, L., Brooks, A., Rhee, G., Wadsley, J., Jonsson, P., Willman, B., Stinson, G., Quinn, T., & Madau, P. 2010, Nature, 463, 203

Hopkins, P. F., Keres, D., Onorbe, J., Faucher-Giguere, C.-A., Quataert, E., Murray, N., & Bullock, J. S. 2013, ArXiv e-prints

Hopkins, P. F., Quataert, E., & Murray, N. 2011, MNRAS, 417, 950

Hopkins, P. F., Richards, G. T., & Hernquist, L. 2007, ApJ, 654, 731

Iliev, I. T., Ciardi, B., Alvarez, M. A., Maselli, A., Ferrara, A., Gnedin, N. Y., Mellema, G., Nakamoto, T., Norman, M. L., Razoumov, A. O., Rijkhorst, E.-J., Ritzerveld, J., Shapiro, P. R., Susa, H., Umemura, M., & Whalen, D. J. 2006a, MNRAS, 371, 1057

Iliev, I. T., Mellema, G., Pen, U.-L., Merz, H., Shapiro, P. R., & Alvarez, M. A. 2006b, MNRAS, 369, 1625

Iliev, I. T., Whalen, D., Mellema, G., Ahn, K., Baek, S., Gnedin, N. Y., Kravtsov, A. V., Norman, M., Raicevic, M., Reynolds, D. R., Sato, D., Shapiro, P. R., Semelin, B., Smidt, J., Susa, H., Theuns, T., & Umemura, M. 2009, MNRAS, 400, 1283

Kaurov, A. A. & Gnedin, N. Y. 2013, ApJ, 771, 35

Khokhlov, A. M. 1998, JCPh, 143, 519

Kravtsov, A. V. 1999, PhD thesis, New Mexico State University

—. 2003, ApJ, 590, L1

—. 2009, ArXiv:0906.3295

Kravtsov, A. V., Klypin, A., & Hoffman, Y. 2002, ApJ, 571, 563

Kuhlen, M. & Faucher-Giguère, C.-A. 2012, MNRAS, 423, 862

Leitherer, C., Schaerer, D., Goldader, J. D., Delgado, R. M. G., Robert, C., Kune, D. F., de Mello, D. F., Devost, D., & Heckman, T. M. 1999, ApJS, 123, 3

Leroy, A. K., Bigiel, F., de Blok, W. J. G., Boissier, S., Bolatto, A., Brinks, E., Madore, B., Munoz-Mateos, J.-C., Murphy, E., Sandstrom, K., Schruba, A., & Walter, F. 2012, AJ, 144, 3

Leroy, A. K., Walter, F., Brinks, E., Bigiel, F., de Blok, W. J. G., Madore, B., & Thornley, M. D. 2008, AJ, 136, 2782

Leroy, A. K., Walter, F., Sandstrom, K., Schruba, A., Munoz-Mateos, J.-C., Bigiel, F., Bolatto, A., Brinks, E., de Blok, W. J. G., Meidt, S., Rix, H.-W., Rosolowsky, E., Schinnerer, E., Schuster, K.-F., & Usero, A. 2013, ArXiv e-prints

McQuinn, M., Lidz, A., Zahn, O., Dutta, S., Hernquist, L., & Zaldarriaga, M. 2007, MNRAS, 377, 1043

Mesinger, A. & Furlanetto, S. 2007, ApJ, 669, 663

Mesinger, A., Furlanetto, S., & Cen, R. 2011, MNRAS, 411, 955

Mitra, S., Choudhury, T. R., & Ferrara, A. 2011, MNRAS, 413, 1569

—. 2012, MNRAS, 419, 1480

Muratov, A. L., Gnedin, O. Y., Gnedin, N. Y., & Zemp, M. 2013a, ApJ, 772, 106

—. 2013b, ApJ, 773, 19

Oesch, P. A., Bouwens, R. J., Illingworth, G. D., Gonzalez, V., Trenti, M., van Dokkum, P. G., Franx, M., Labbé, I., Carollo, C. M., & Magee, D. 2012, ApJ, 759, 135

Oesch, P. A., Bouwens, R. J., Illingworth, G. D., Labbé, I., Franx, M., van Dokkum, P. G., Trenti, M., Stiavelli, M., Gonzalez, V., & Magee, D. 2013a, ApJ, 773, 75

Oesch, P. A., Bouwens, R. J., Illingworth, G. D., Labbe, I., Smit, R., van Dokkum, P. G., Momcheva, I., Ashby, M. L. N., Fazio, G. G., Huang, J., Willner, S. P., Gonzalez, V., Magee, D., Trenti, M., Brammer, G. B., Skelton, R. E., & Spitler, L. R. 2013b, ArXiv e-prints

Pawlik, A. H., Schaye, J., & van Scherpenzeel, E. 2009, MNRAS, 394, 1812

Richards, G. T., Lacy, M., Storrie-Lombardi, L. J., Hall, P. B., Gallagher, S. C., Hines, D. C., Fan, X., Papovich, C., Vanden Berk, D. E., Trammell, G. B., Schneider, D. P., Vestergaard, M., York, D. G., Jester, S., Anderson, S. F., Budavári, T., & Szalay, A. S. 2006, ApJS, 166, 470

Ricotti, M., Gnedin, N. Y., & Shull, J. M. 2002a, ApJ, 575, 33

—. 2002b, ApJ, 575, 49

Robertson, B. E., Furlanetto, S. R., Schneider, E., Charlot, S., Ellis, R. S., Stark, D. P., McLure, R. J., Dunlop, J. S., Koekemoer, A., Schenker, M. A., Ouchi, M., Ono, Y., Curtis-Lake, E., Rogers, A. B., Bowler, R. A. A., & Cirasuolo, M. 2013, ApJ, 768, 71

Rogers, A. B., McLure, R. J., Dunlop, J. S., Bowler, R. A. A., Curtis-Lake, E. F., Dayal, P., Faber, S. M., Ferguson, H. C., Finkelstein, S. L., Grogin, N. A., Hathi, N. P., Kocevski, D., Koekemoer, A. M., & Kurczynski, P. 2013, ArXiv e-prints

Rudd, D. H., Zentner, A. R., & Kravtsov, A. V. 2008, ApJ, 672, 19

Schaye, J., Vecchia, C. D., Booth, C. M., Wiersma, R. P. C., Theuns, T., Haas, M. R., Bertone, S., Duffy, A. R., McCarthy, I. G., & van de Voort, F. 2009, MNRAS, 1888

Schenker, M. A., Robertson, B. E., Ellis, R. S., Ono, Y., McLure, R. J., Dunlop, J. S., Koekemoer, A., Bowler, R. A. A., Ouchi, M., Curtis-Lake, E., Rogers, A. B., Schneider, E., Charlot, S., Stark, D. P., Furlanetto, S. R., & Cirasuolo, M. 2013, ApJ, 768, 196

Shull, J. M. & Venkatesan, A. 2008, ApJ, 685, 1

Sobacchi, E. & Mesinger, A. 2014, ArXiv e-prints

Songaila, A. & Cowie, L. L. 2010, ApJ, 721, 1448

Stinson, G. S., Brook, C., Macciò, A. V., Wadsley, J., Quinn, T. R., & Couchman, H. M. P. 2013, MNRAS, 428, 129

Stinson, G. S., Dalcanton, J. J., Quinn, T., Gogarten, S. M., Kaufmann, T., & Wadsley, J. 2009, MNRAS, 395, 1455

Tacconi, L. J., Neri, R., Genzel, R., Combes, F., Bolatto, A., Cooper, M. C., Wuyts, S., Bournaud, F., Burkert, A., Comerford, J., Cox, P., Davis, M., Förster Schreiber, N. M., García-Burillo, S., Gracia-Carpio, J., Lutz, D., Naab, T., Newman, S., Omont, A., Saintonge, A., Shapiro Griffin, K., Shapley, A., Sternberg, A., & Weiner, B. 2013, ApJ, 768, 74

Trac, H. & Cen, R. 2007, ApJ, 671, 1
Trac, H., Cen, R., & Loeb, A. 2008, ApJ, 689, L81
Trac, H. & Gnedin, N. Y. 2009, ArXiv e-prints
Venkatesan, A. & Benson, A. 2011, MNRAS, 417, 2264
Weingartner, J. C. & Draine, B. T. 2001, ApJ, 548, 296
White, R. L., Becker, R. H., Fan, X., & Strauss, M. A. 2003, AJ, 126, 1
Wiersma, R. P. C., Schaye, J., & Smith, B. D. 2009, MNRAS, 393, 99
Willott, C. J., McLure, R. J., Hibon, P., Bielby, R., McCracken, H. J., Kneib, J.-P., Ilbert, O., Bonfield, D. G., Bruce, V. A., & Jarvis, M. J. 2013, AJ, 145, 4
Wise, J. H. & Abel, T. 2008, ApJ, 684, 1
Wise, J. H. & Cen, R. 2009, ApJ, 693, 984
Wise, J. H., Turk, M. J., Norman, M. L., & Abel, T. 2012, ApJ, 745, 50
Zahn, O., Lidz, A., McQuinn, M., Dutta, S., Hernquist, L., Zaldarriaga, M., & Furlanetto, S. R. 2007a, ApJ, 654, 12
—. 2007b, ApJ, 654, 12
Zahn, O., Mesinger, A., McQuinn, M., Trac, H., Cen, R., & Hernquist, L. E. 2011, MNRAS, 414, 727
Zhou, J., Guo, Q., Liu, G.-C., Yue, B., Xu, Y.-D., & Chen, X.-L. 2013, Research in Astronomy and Astrophysics, 13, 373